International Journal of Biological Macromolecules 248 (2023) 125961



Contents lists available at ScienceDirect

International Journal of Biological Macromolecules

journal homepage: www.elsevier.com/locate/ijbiomac

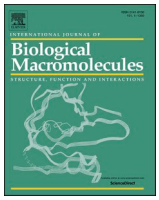



Experimental and theoretical approaches to interactions between DNA and purine metabolism products

Alper Fitoz, Zehra Yazan *

Ankara University, Faculty of Science, Department of Chemistry, 06560, Turkey

ARTICLE INFO

Keywords:
DFT
NBO
Molecular docking
DNA-interaction
Voltammetry

ABSTRACT

Deoxyribonucleic acid (DNA) is a significant target for small organic and inorganic drug molecules. Understanding the DNA interaction mechanism of these molecules is vital for new drug designs. In this work, interactions between xanthine (XT), theophylline (TP), and theobromine (TB) with calf-thymus double-strained DNA (dsDNA) were monitored via an experimental and theoretical approach. Experimentally, cyclic voltammetry (CV) and differential pulse voltammetry (DPV) techniques were used on the surface of the NiO/MWCNT/NNaM/PGE electrochemical platform in vitro. Kinetic parameters, including diffusion coefficients, surface concentrations, and standard heterogeneous rate constants, were measured in the absence and presence of DNA using scan rate studies. In the presence of DNA, kinetic parameters were observed to be reduced significantly. Thermodynamic parameters, such as DNA binding constants and standard free Gibbs energies, were calculated for each molecule using the CV and DPV techniques. Both techniques suggested a binding affinity order of XT > TB > TP. Theoretically, density functional theory was applied for geometry optimization, natural bond orbital analyses, and molecular orbital energies of XT, TP, and TB. Experimental and theoretical binding affinities confirm each other. The most energetically stable ligand-DNA complexes expressed that XT, TP, and TB interact with dsDNA via minor groove binding mode, using mostly hydrogen bonds.

1. Introduction

Deoxyribonucleic acid (DNA) is a vital molecule for living organisms. It contains hereditary information, synthesizes proteins and enzymes, performs transcription processes, etc. [1,2]. The binding of small organic or inorganic ligands can disrupt its double helix structure [3]. As a result, DNA cannot perform its normal function, and this leads to mutations, causing various hereditary diseases in living things [4]. Besides, these DNA mutations can simply cause cancer [5]. These mutations result in observable thermodynamical and functional property changes in DNA structure [6]. These observations might help in understanding interaction mechanisms and, therefore, designing effective drugs for the treatment of DNA-related diseases.

Xanthine (XT) (IUPAC Name: 3,7-dihydro-purine-2,6-dione) is a purine metabolism product and is found in tissues and body fluids, including blood and urine [7]. XT is also used as an indicator for estimating fish freshness since it is an important metabolite from the breakdown of adenosine triphosphate (ATP) in fish meat [8]. Theophylline (TP, IUPAC Name: 1,3-dimethyl-7H-purine-2,6-dione) and theobromine (TB, IUPAC Name: 3,7-dimethyl-1H-purine-2,6-dione) are purine molecules that are also commonly found in the human diet and body fluids [9,10]. XT, TP, and TB have biological effects, such as their ability to transform each other into the liver [11]. The purine-DNA interaction may cause a defect in purine nucleotide metabolism [12].

Small aromatic molecules usually interact with DNA in intercalation mode. Intercalation may occur in three ways: the first one is binding between DNA base pairs in a double-helix structure; the second one is groove bonding; and the last one is non-specific electrostatic binding with a negatively charged nucleic acid-phosphate structure [13]. Determining the DNA interaction types of these biomolecules included in commonly adopted diets, medications, and body fluids could provide information for assessing their mutation impacts on DNA structure and supporting new drug designs.

Nuclear magnetic resonance [14], UV spectroscopy [15–22], microcalorimetry [6,16,23], etc. have been used to determine ligand-macromolecule (DNA, RNA, etc.) interactions. Despite their accuracy, these techniques have disadvantages to consider, such as yielding considerable amounts of toxic solution waste, having interference

* Corresponding author.
E-mail address: zdurmus@science.ankara.edu.tr (Z. Yazan).

https://doi.org/10.1016/j.ijbiomac.2023.125961
Received 15 March 2023; Received in revised form 13 June 2023; Accepted 12 July 2023
Available online 23 July 2023
0141-8130/© 2023 Elsevier B.V. All rights reserved.

effects, and requiring time-consuming preprocesses [24,25]. On the other hand, electrochemical techniques offer researchers the ability to investigate such interactions with rapid and reproducible measurements [12,26]. Glassy carbon [27], carbon paste [28], pencil graphite [29], and boron-doped diamond [30] electrodes have been used in the literature to monitor these interactions. Pencil graphite electrodes (PGEs) are exceptional electrochemical sensor platforms due to their low cost, disposable nature, and ease of surface modification. Besides, surface modifications make PGE sensors more sensitive to biomolecules [29,31]. In addition to experimental methods, computational methods such as molecular docking [32] and density functional theory (DFT) [33] provide critical information about the structure of DNA-ligand complexes before experiment sequences. Therefore, researchers can reduce both time and experimental waste by having preliminary knowledge of molecular structures and interactions.

A review of the literature revealed that the DNA binding constants of XT, TP, and TB to DNA have never been calculated using electrochemical techniques. Several publications used UV spectroscopy to investigate the DNA interactions of TP and TB. Johnson et al. [34] calculated the DNA binding constants for theophylline, theobromine, and caffeine using UV spectroscopy in the presence of Mg^{2+} ions as $3.5 \times 10^3\ M^{-1}$, $1.1 \times 10^3\ M^{-1}$, and $3.8 \times 10^3\ M^{-1}$, respectively. Nafisi et al. [35] calculated the DNA binding constants of caffeine and theophylline using UV spectroscopy as $9.7 \times 10^3\ M^{-1}$ and $1.7 \times 10^4\ M^{-1}$, respectively. Nemcekova et al. [36] investigated the interaction between TP and dsDNA using electrochemical techniques without calculating the binding constant. The DNA interaction of XT is examined in this paper for the first time. The DNA binding constants for XT, TP, and TB are calculated for the first time using electrochemical techniques and molecular docking.

In this paper, the DNA interactions of XT, TP, and TB were investigated using experimental and theoretical techniques. Voltammetric techniques (cyclic (CV) and differential pulse voltammetry (DPV)) were used to calculate kinetic and thermodynamic parameters under optimized conditions (0.1 M Britton-Robertson buffer, pH: 4.8) on the NiO/MWCNT/NNaM/PGE surface in vitro. The formation of each DNA complex was demonstrated with diffusion coefficients, surface concentrations, and standard heterogeneous rate constants in the presence and absence of DNA for each analyte. The interaction type of each molecule was evaluated, and DNA binding constants for each molecule were calculated using CV and DPV techniques. XT, TP, and TB do not interact between base pairs of dsDNA according to the binding constants and oxidation potential shifts. Molecular docking poses for each molecule express that DNA interactions are governed via minor groove bonding mode. In addition, NBO analyses confirm the formation of hydrogen bonds.

2. Experimental

2.1. Chemicals and solutions

Sigma-Aldrich provided xanthine (99 %), theophylline (99 %), theobromine (98 %), and calf-thymus double-stranded DNA (sodium salt). Sigma-Aldrich also supplied the boric acid (99.5 %), acetic acid (100 %), and phosphoric acid (85.0–88.0 %) used to prepare the BR buffer, as well as the HCl (36.5–38.0 %). The MERK company provides NaOH (%97).

Double-distilled pure water was produced by a mpMINIpure distiller. The Britton-Robinson (BR) buffer solution was prepared to contain 0.04 M of acetic acid, boric acid, and phosphoric acid as an electrolyte solution. pH values of electrochemical experiments were adjusted with 0.01 M, 0.1 M, and 2.0 M HCl and NaOH solutions using the HANNA HI 2211 pH/ORP meter.

A DNA stock solution was prepared to contain 1000 mg of calf-thymus dsDNA per liter of double-distilled water. The resulting solution's concentration was determined using UV spectroscopy ($\lambda_{max} = 260$ nm) as 2×10^{-3} M [29].

2.2. Electrochemical measurements

Voltametric measurements (CV and DPV) were performed with the CHI 760B electrochemical workstation. A three-electrode system was used on a BASC3 cell stand for experiments. The Ag/AgCl (BASi MF-2052), Pt wire (BASi MW-1032), and NiO/MWCNT/NNaM/PGE were used as a reference, auxiliary, and working electrode, respectively. The preparation, surface analysis, and electrochemical performance of the NiO/MWCNT/NNaM/PGE electrochemical sensor platform (active surface area: $0.678 \pm 0.016\ cm^2$) were utilized in our previous work [9]. The NiO/MWCNT/NNaM/PGE electrochemical platform consists of a bare PGE surface modified by nickel oxide (NiO) nanoparticles, multi-walled carbon nanotubes (MWCNT), and a nano-clay structure of sodium montmorillonite (NNaM).

CV measurements were performed at various scan rates (v: 25–300 mV/s). Potential scans for XT, TP, and TB are (+0.6)–(+1.4)–(+0.6 V), (+1.0)–(+1.5)–(+1.0) V and (+1.2)–(+1.8)–(+1.2) V, respectively. DPV measurements were performed under these conditions: potential increase: 0.004 V, amplitude: 0.05 V, pulse width: 0.05 s, sample width: 0.0167 s, and pulse duration: 0.5 s. Potential scans for XT, TP, and TB are (+0.7)–(+1.1) V, (+1.0)–(+1.4) V, and (+1.2)–(+1.7) V, respectively.

2.3. Electrochemical evaluation of DNA interactions

The DNA interactions of XT, TP, and TB were evaluated via their oxidation peak currents in the absence and presence of dsDNA using CV and DPV. The measurements were applied after a certain interaction time (90 s.). Transferred electron numbers (n) were determined using the slope of E_{pa}–log v plots and the Laviron Equation (Eq. (1)). The standard heterogeneous rate constants (k^0) of XT, TP, and TB and their DNA complexes were calculated using the slope of E_{pa}–ln v plots and Eq. (1):

$$E_{pa} = E^0 + \left(\frac{2.303RT}{\alpha nF}\right) log\left(\frac{2.303RTk^0}{\propto nF}\right) + \left(\frac{2.303RT}{\propto nF}\right) logv \quad (1)$$

E_{pa} (V), E^0 (V), R (8.314 J/K.mol), T (Kelvin), n, F (C/mol), k^0, and v (V/s) denote the oxidation potential, formal potential, ideal gas constant, temperature, electron transfer coefficient, transferred electron number, Faraday constant, standard heterogeneous rate constant, and scan rate, respectively [37,38]. The higher slope value of E_{pa}–log v plots for each ligand (XT, TP, and TB) is attributed to the presence of abundant electrons, which might change the preferred binding sites of the molecules [39].

The diffusion coefficient values were calculated using the slope of the i_{pa}–$v^{1/2}$ plots and the Randles-Sevcik Equation as follows:

$$i_{pa} = \left(2.687 \times 10^5\right) \times n^{\frac{3}{2}} \times D^{\frac{1}{2}} \times A \times C \times v^{\frac{1}{2}} \quad (2)$$

Herein, i_{pa} (mA), n, D (cm^2/s), A (cm^2), C (mol/cm^3), and v (mV/s) represent the oxidation peak current, transferred electron number, diffusion coefficient, the active surface area of the working electrode, concentration of the analyte, and scan rate [40].

The surface concentration values were calculated using the slope of i_{pa}–v plots according to the following equation:

$$i_{pa} = \frac{n^2 \times F^2}{4 \times R \times T} \times A \times v \times \Gamma \quad (3)$$

Herein, Γ (mol/cm^2) represents the surface concentration of an analyte. Other symbols were discussed in the preceding sections [41].

The binding constants were measured via the addition of various DNA concentrations (10, 20, 40, 60, and 80 μM) in the presence of constant ligand concentrations (CV: C_{XT}: 100 μM, C_{TP}: 200 μM, and C_{TB}: 250 μM and DPV: C_{XT}: 40 μM, C_{TP}: 70 μM, and C_{TB}: 90 μM) according to the following equation:

$$log\left[\frac{i_{L-DNA}}{i_L - i_{L-DNA}}\right] = logK_{L-DNA} + log\left[\frac{1}{C_{DNA}}\right] \quad (4)$$

Herein, L, $K_{L\text{-}DNA}$, i_L, and $i_{L\text{-}DNA}$ represent the ligand molecule to be bound to DNA, the binding constant of the L-DNA complex, the anodic peak current of the ligand in DNA-free solution, and the anodic peak currents of the ligand in DNA-added solution, respectively [42]. The binding constants were calculated using the interception of the log [1/C_{DNA}]–log [$i_{L\text{-}DNA}$ / i_L – $i_{L\text{-}DNA}$] plots for each analyte.

The standard binding free Gibbs Energies (ΔG_b^0) of XT-DNA, TP-DNA, and TB-DNA complexes were calculated from the following equation:

$$\Delta G_b^0 = -RTlnK_{L-DNA} \quad (5)$$

Herein, R, T, and $K_{L\text{-}DNA}$ are the ideal gas constant (J/K.mole), the absolute temperature (Kelvin, K), and the binding constant of the L-DNA complex, respectively [43].

2.4. DFT and molecular docking studies

Geometry optimization and NBOs analyses were carried out with DFT, applying Becke's 3-parameter combined with the Lee-Yang-Parr method (B3LYP) with a 6-31G (d,p) basis set for XT, TP, and TB ligands in the gas phase. Optimized structures were used for molecular docking studies. To calculate the global reactivity parameters of each ligand, including HOMO, LUMO energies, and the energy gap (ΔE) calculated using the time-dependent DFT (TD-DFT) technique. The visualization of the optimized geometries and the generation of their pdb files were accomplished with the Avogadro software [44] for XT, TP, and TB. These calculations were performed in the Gaussian 09 software [45]. Ionization potential (*I*), electron affinity (*A*), and electronic chemical potential (μ_e) values are calculated from E_{HOMO} and E_{LUMO} values according to the following equations [46]:

$$I = -E_{HOMO} \quad (6)$$

$$A = -E_{LUMO} \quad (7)$$

$$\mu_e = E_{HOMO} + E_{LUMO}/2 \quad (8)$$

Global hardness (η), softness (S), electronegativity (χ), and electrophilicity index (ω) are calculated using the following equations [47]:

$$\eta = I - A/2 \quad (9)$$

$$S = 1/2\eta \quad (10)$$

$$\chi = I + A/2 \quad (11)$$

$$\omega = \mu^2/2\eta \quad (12)$$

The molecular docking process was applied via AutoDock v. 4.2.6 software [48] in 50 runs to obtain the most stable DNA-Ligand structures of XT, TP, and TB with the use of the Lamarckian Genetic Algorithm and blind docking. The crystal structure of dsDNA was downloaded from the protein data bank (PDB ID: 1BNA). Just before the docking applications, water and ligand molecules were removed from the structure using the AutoDockTools v. 1.5.7 software [48]. The visualization of 3D DNA-ligand complexes and 2D interaction maps were created in the BIOVIA Discovery Studio software [49].

3. Results

3.1. Experimental part

3.1.1. Scan rate studies

CV voltammograms of 100 μM XT, 250 μM TP, and 450 μM TB in the absence and presence of 50 μM DNA at a 100 mV/s scan rate are represented in Fig. S1. Anodic peak currents of XT, TP, and TB were observed at (+1.010 ± 0.004), (+1.292 ± 0.005), and (+1.560 ± 0.007) V, respectively, with an irreversible redox reaction. Anodic peak currents of XT, TP, and TB decreased, while E_{pa} values remained relatively constant after the addition of dsDNA (Fig. S1).

Scan rate analysis was recorded for each analyte in the absence and presence of 50 μM dsDNA at various scan rates (*v*: 25, 50, 100, 150, 200, and 250 mV/s). The i_{pa}–$v^{1/2}$, i_{pa}–*v*, and E_{pa}–ln *v* plots of XT, TP, and TB were evaluated in the absence (Fig. S2) and presence (Fig. S3) of dsDNA. Firstly, the transferred electron numbers (n) of XT, TP, and TB were calculated on the NiO/MWCNT/NNaM/PGE electrochemical sensor platform during the oxidation process. n values for XT, TP, and TB values were determined using Eq. (1) and E_{pa}–log *v* plots (Fig. S2a) as 2.24 (± 0.11), 2.33 (± 0.11), and 2.26 (± 0.09), respectively, assuming α 0.5 for an irreversible process [9].

The *D* values for XT, TP, and TB were calculated using Eq. (2) and the slope of the i_{pa}–$v^{1/2}$ plots in the absence (Fig. S2b) and presence (Fig. S3a) of dsDNA. Γ values of XT, TP, and TB are calculated using Eq. (3) and the slope of i_{pa}–*v* plots in the absence (Fig. S2c) and presence (Fig. S3b) of dsDNA. k^0 values are calculated using Eq. (1) and the slope of E_{pa}–ln *v* plots in the absence (Fig. S2d) and presence (Fig. S3c) of dsDNA, assuming α values of 0.5 for an irreversible oxidation process. Kinetic parameters in the absence and presence of dsDNA are represented in Table 1. *D* and Γ values were significantly reduced after dsDNA addition for each analyte. These decreases can contribute to the formation of non-redox ligand-DNA complexes. k^0 values that are slightly reduced after dsDNA addition for each analyte indicate that the formation of complex structures is relatively slow (Table 1).

3.1.2. Binding constants of DNA complexes

CV and DPV techniques were applied to calculate the binding constants of XT-DNA, TP-DNA, and TB-DNA complexes. The CV technique was applied at a 100 mV/s scan rate (other optimum conditions are described in the experimental section). DNA was added to the electrochemical cell in five increasing concentrations (10, 20, 40, 60, and 80 μM). Figs. 1 and 2 represent CV and DP voltammograms, and log 1/[DNA]–log [log $i_{L\text{-}DNA}$/ i_L–$i_{L\text{-}DNA}$] plots are shown as insets. Eq. (4) and the interception of log 1/[DNA]-log [log $i_{L\text{-}DNA}$/ i_L–$i_{L\text{-}DNA}$] plots were used to calculate binding constants (K_b) for XT-DNA, TP-DNA, and TB-DNA complexes. Relatively small K_b values obtained from CV measurements suggested that binding to ds-DNA for each analyte involves electrostatic interactions and/or groove binding modes. Similar trends were obtained by using the DPV technique (Table 2). The difference between CV and DPV techniques in terms of K_b values is likely due to the higher sensitivity of the DPV technique towards biomolecules [42].

The standard Gibbs free energies (ΔG^0) of XT-DNA, TP-DNA, and TB-DNA complexes are calculated using Eq. (5). Table 2 represents the calibration parameters of log 1/[DNA]–log [log $i_{L\text{-}DNA}$/ i_L–$i_{L\text{-}DNA}$] plots and calculated K_b and ΔG^0 values for DNA complexes. E_{pa} values did not shift considerably after DNA additions using CV and DPV. Relatively small K_b values indicated that XT, TP, and TB do not interact between dsDNA base pairs. ΔG^0 values express that the interactions of XT, TP, and TB with dsDNA are thermodynamically spontaneous. The binding affinity order to dsDNA is XT > TB > TP for both CV and DPV techniques.

Table 1
Kinetic parameters calculated in the absence and presence of dsDNA from scan rate analysis.

Kinetic parameters	*D* (cm^2/s)	Γ (mol/cm^2)	k^0 (s^{-1})
XT	$2.47 \pm 0.43 \times 10^{-2}$	$1.57 \pm 0.17 \times 10^{-10}$	$1.18 \pm 0.36 \times 10^{2}$
TP	$6.09 \pm 0.99 \times 10^{-4}$	$5.79 \pm 0.63 \times 10^{-11}$	$1.23 \pm 0.36 \times 10^{2}$
TB	$6.35 \pm 0.88 \times 10^{-4}$	$6.15 \pm 0.60 \times 10^{-11}$	$1.19 \pm 0.31 \times 10^{2}$
XT-DNA	$8.71 \pm 0.74 \times 10^{-3}$	$9.39 \pm 0.98 \times 10^{-11}$	$8.79 \pm 0.54 \times 10^{1}$
TP-DNA	$5.95 \pm 0.96 \times 10^{-5}$	$1.45 \pm 0.15 \times 10^{-11}$	$7.64 \pm 0.29 \times 10^{1}$
TB-DNA	$8.19 \pm 1.11 \times 10^{-5}$	$2.15 \pm 0.23 \times 10^{-11}$	$9.24 \pm 0.78 \times 10^{1}$

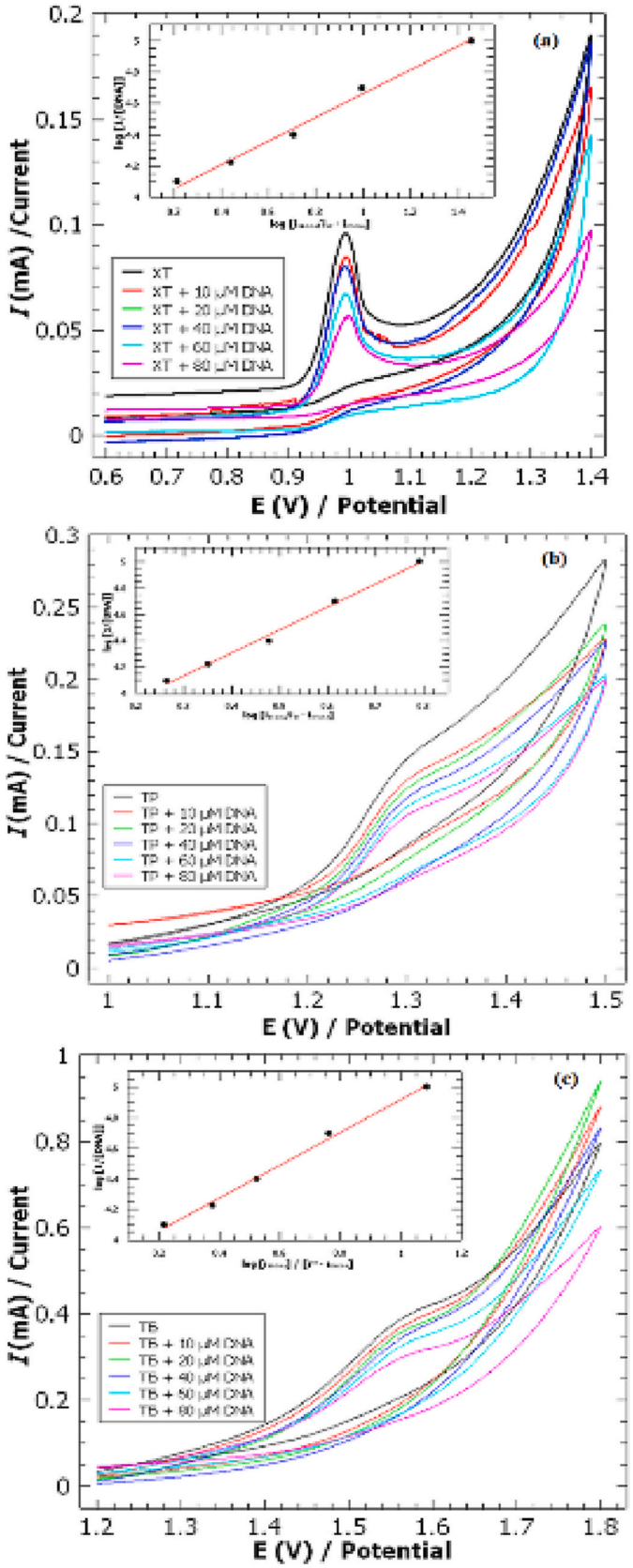

Fig. 1. CV voltammograms of (a) 100 µM XT, (b) 200 µM TP, and (c) 250 µM TB with varying dsDNA concentrations, and log 1/[DNA]–log [log $i_{L\text{-}DNA}$ / i_L–$i_{L\text{-}DNA}$] plots as insets.

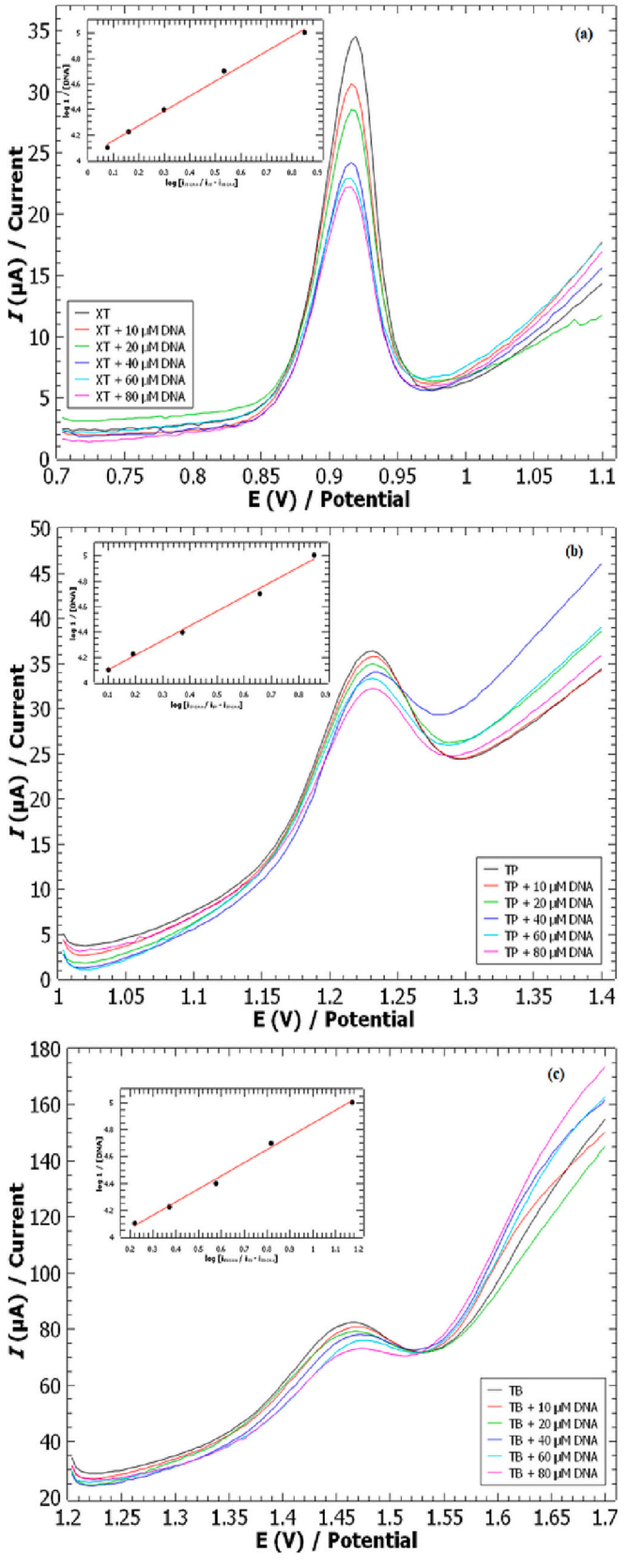

Fig. 2. DP voltammograms of (a) 40 µM XT, 70 µM TP, and 90 µM TB with varying dsDNA concentration, and (d) log 1/[DNA]–log [log $i_{L\text{-}DNA}$ / i_L–$i_{L\text{-}DNA}$] plots as insets

Table 2
Calibration parameters of log [1/[DNA]]–log [$i_{L\text{-}DNA}/i_L$–$i_{L\text{-}DNA}$] plots and calculated K_b and ΔG^0 values for XT-DNA, TP-DNA, and TB-DNA complexes.

Parameters		Slope	Interception	R^2	K_b (M^{-1})	ΔG^0 (kJ/mol)
CV	XT	0.7556 ± 0.0403	3.9095 ± 0.0354	0.9914	8.12 ± 0.66 × 10^3	−22.31 ± 0.04
	TP	1.7412 ± 0.0766	3.6126 ± 0.0409	0.9942	4.10 ± 0.37 × 10^3	−20.62 ± 0.04
	TB	1.0774 ± 0.0449	3.8437 ± 0.0299	0.9938	6.98 ± 0.48 × 10^3	−21.94 ± 0.03
DPV	XT	1.6596 ± 0.0532	4.0345 ± 0.0253	0.9971	1.08 ± 0.12 × 10^4	−23.03 ± 0.03
	TP	0.9736 ± 0.0393	3.8665 ± 0.0282	0.9951	7.35 ± 0.48 × 10^3	−22.07 ± 0.03
	TB	1.1561 ± 0.0509	3.9782 ± 0.0265	0.9942	9.51 ± 0.58 × 10^3	−22.71 ± 0.03

3.2. Theoretical part

3.2.1. Geometry optimization

Geometry optimizations for XT, TP, and TB were calculated using DFT/B3LYP/631-G (d, p) level theory. The optimized structures (Fig. S4) were used for molecular docking analysis later. On the other hand, geometry optimization provides valuable data such as Mulliken charges. For each molecule, all the nitrogen and oxygen atoms in the structure have highly negative charges. In the cases of TP and TB, the *N*-methyl carbon atoms provide extra negative charges. These negatively charged regions indicate potential electron donor sites for XT, TP, and TB. The C1, C2, and C3 atoms and hydrogen atoms that bond to heteroatoms (N—H type) in each molecule have significantly positive charges, indicating potential acceptor sites for XT, TP, and TB. are also positively charged for XT, TP, and TB (Table S1).

3.2.2. Molecular orbitals and global reactivity parameters

Molecular orbital energies were calculated using TD-DFT for each molecule. E_{HOMO}, E_{LUMO}, ΔE, and related global reactivity parameters are represented in Table 3. Since E_{HOMO} and E_{LUMO} values express the electron donor and acceptor ability of a molecule, energetically the most favorable electron donor and acceptor molecules are TB and XT, respectively [50]. TB is the energetically most active molecule according to the ΔE values. Global activity parameters also express the same trend (Table 3).

3.2.3. NBOs analyses

NBO population analysis provides a better estimate for partial atomic charges compared to Mulliken charges [51]. Therefore, the partial charges of atoms in each molecule were determined by NBO analysis. The results are given in Table S1. In general, the partial charge values showed a similar trend to the Mulliken charges; however, some important differences were observed. N—H type hydrogen atoms have significantly more positive partial charges, while O1 and O2 atoms have slightly more negative values for each molecule compared to Mulliken charges. In the case of TP and TB, the negative partial charges of methylated N atoms were significantly reduced compared to those of XT. As a consequence of the methylation of two hetero atoms in the TP and TB structures, XT has significantly more negatively charged hetero atoms and significantly more positively charged N—H type hydrogens, which can serve as H-acceptor and H-donor, respectively.

NBO population analyses also generate valuable data for filled and virtual orbital spaces where H-bonds can form [52]. The stabilization energy of a bond between the donor and acceptor orbitals, E(2), is associated with the interaction between the filled orbital (i) and vacant orbital (j), respectively. E(2) value can be determined using the theory of 'the second order perturbation' from NBO analysis [51]. Non-covalent interactions like hydrogen bonds forming between lone pairs (LP) and anti-bonding orbitals (n-σ*) can be characterized with an E(2) value. A stronger hydrogen-bonded system has a higher E(2) value [53]. A selected summary of donor-acceptor orbitals and interaction E(2) values for XT, TP, and TB are represented in Tables S2, S3, and S4, respectively. Each molecule has strong E(2) values, including σ → σ*, π → π*, n → σ*, and n → π* transitions. Since non-covalent interactions are effective in ligand-DNA interactions, the n → σ* transitions responsible for the formation of H-bonds were discussed.

In general, lone pair (LP) electrons of N1, N2, and N3 in each molecular structure prefer n → π* transitions with high E(2) values (between 57.53 and 61.8 kcal/mol). On the other hand, LP electrons of O1 and O2 in each molecule prefer n → σ* transitions (XT: n2(O1) → σ*(N1–C2) and n2(O2) → σ*(C2–N2), TP: n2(O1) → σ*(N1–C2) and n2(O2) → σ*(C1–N1), TB: n2(O1) → σ*(C2–N2) and n2(O2) → σ*(C1–N1)) with high E(2) values (XT: 27.84 and 29.72; TP: 27.28 and 29.49; TB: 26.94 and 28.70 kcal/mol) where they can form H-bonds. Therefore, O1 and O2 are considered energetically potential H-acceptor sites in each molecule. LP electrons of N4 in each molecule have n(N4) → σ*(N3–C5), n(N4) → LP(N4), and n(N4) → σ*(N3–C5) transitions with 8.28, 8.28, and 8.42 kcal/mol for XT, TP, and TB, respectively, indicating less stable H-acceptor sites. In the XT molecule structure, it has two more N—H type bonds compared to TP and TB. These bonds have σ → σ* transitions (σ(N1−H2) → σ*(C1–O2), σ(N2−H1) → σ*(N2–C2), and σ(N3−H3) → σ*(C4–N3)) with very small E(2) values (0.54, 0.57, and 0.60 kcal/mol) for XT (Table S2) indicating possible H-donors to DNA nucleobases. As a result of having two more *N*-methyl groups, TP and TB have one N—H type bond for each with similar E(2) values (Tables S3 and S4).

The visualization of these mentioned orbitals is represented in Figs. S5, S6, and S7 for XT, TP, and TB, respectively. Electron-donor sites of the XT molecule are localized mostly on the six-membered pyrimidine ring, while electron-acceptor sites of the XT molecule are localized on the whole molecule (Fig. S5). In the case of TP, electron-donor sites localize mostly on the six-membered pyrimidine ring, while electron-acceptor sites of the TP molecule are localized on the whole molecule (Fig. S6). Electron-donor TB sites are located on the whole molecule, while electron-acceptor sites of TB are localized on the whole molecule (Fig. S7).

Table 3
Calculated theoretical parameters.

DFT	XT	TP	TB
E_{HOMO} (a.u.)	−0.23422	−0.22371	−0.22244
E_{LUMO} (a.u.)	−0.04075	−0.03545	−0.03641
ΔE (a.u.)	0.19347	0.18826	0.18603
μ_e (a.u.)	−0.13749	−0.13223	−0.12943
I (a.u.)	0.23422	0.22371	0.22244
A (a.u.)	0.04075	0.03545	0.03641
η (a.u.)	0.09674	0.09413	0.09301
S (a.u.)	5.16876	5.31180	5.37548
χ (a.u.)	0.13749	0.13223	0.12943
ω (a.u.)	0.09770	0.09288	0.09005
Molecular Docking	XT-DNA	TP-DNA	TB-DNA
Inhibition constant (nm)	623.59	941.99	668.29
ΔG_b^0 (kcal/mol)	−8.47	−8.22	−8.42

3.2.4. Molecular docking

Molecular docking analyses were applied using the dsDNA structure (1bna) and optimized structures of each ligand. Fig. S8 represents the formation of (a) XT-DNA, (b) TP-DNA, and (c) TB-DNA complexes. Each ligand molecule interacts with the minor groove regions of dsDNA according to docking images. In more detail, 2D and 3D visualizations of the interactions are represented in Fig. 3 for each complex. XT, TP, and TB interact with both helix structures (A and B) of dsDNA (1bna) via non-covalent bindings.

XT interacts with dsDNA A-helix via three conventional hydrogen bonds (Guanine10–H3, Guanine10–O2, and Cythozine11–H2) as both H-donor and acceptor. XT interacts with dsDNA B-helix via one conventional H-bond (Adenine17–N4), and one π-donor hydrogen bond

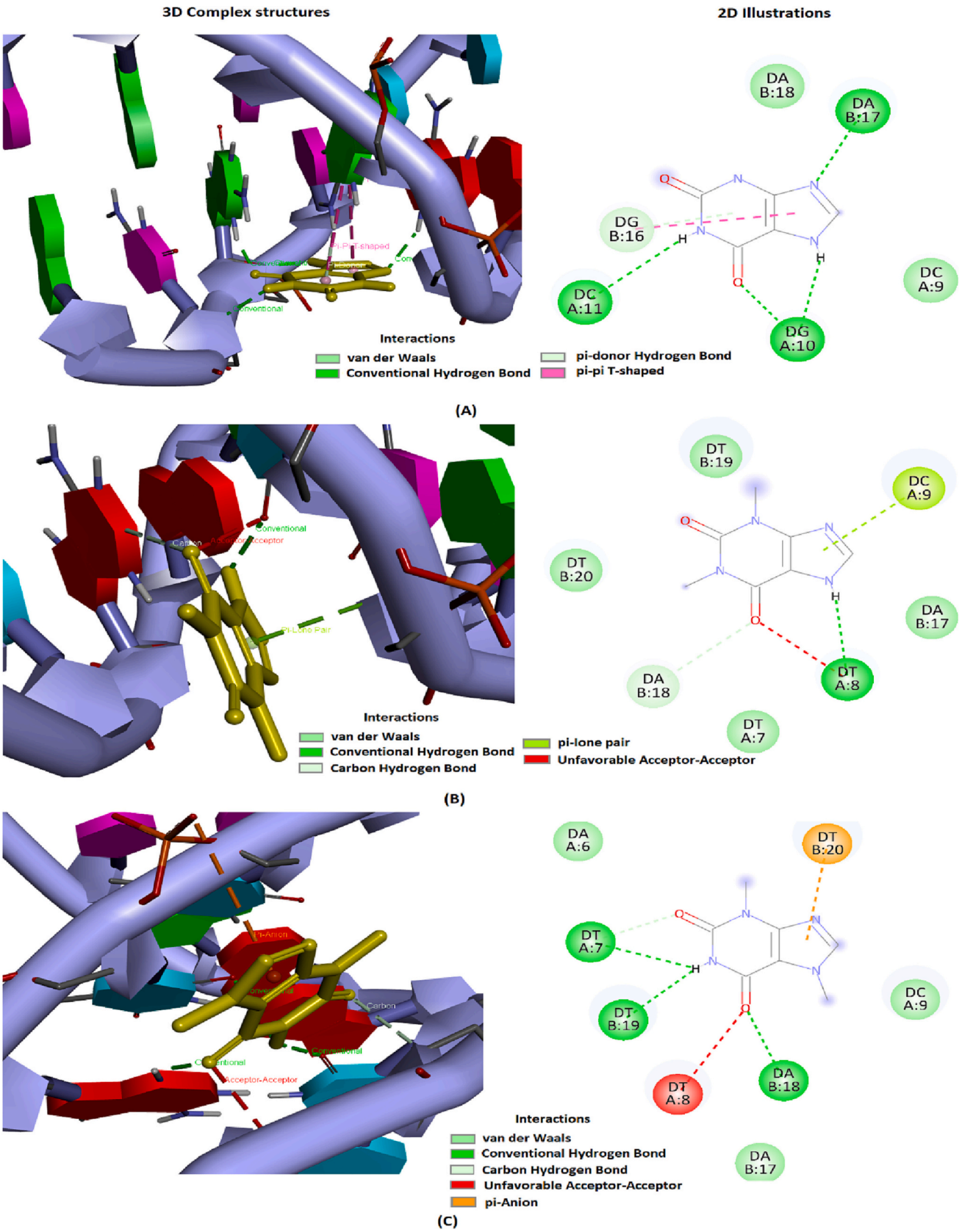

Fig. 3. 3D complex structures and 2D interaction maps of XT-DNA, TP-DNA, and TB-DNA.

(Guanine16–imidazole ring) as H-acceptor (Fig. 3A). TP interacts with dsDNA A-helix via one conventional H-bond (Tymine8–H1) as H-donor. TP interacts with dsDNA B-helix via one carbon-hydrogen bond (Adenine18–O2) as H-acceptor (Fig. 3B). TB interacts with dsDNA A-helix via a conventional H-bond (Tymine7–H8), and one carbon-hydrogen bond (Tymine7–O1) as both H-donor and acceptor. TB interacts with dsDNA B-helix via two conventional H-bonds (Adenine18–O2 and Tymine19–H8) as both H-donor and acceptor and one electrostatic π-anion interaction (phosphate backbone of Tymine20–imidazole ring) (Fig. 3C).

Binding energies (ΔG_b^0) and inhibition constants obtained from molecular docking analyses are represented in Table 3 for each DNA complex. The binding affinity order is XT > TB > TP in agreement with voltammetric results. Due to having more H-bonds, XT and TB's affinities to dsDNA are slightly higher than those of TP. Complex DNA structures also suggested that XT, TP, and TB interact via dsDNA in a minor groove binding mode using mostly H-bonds [54,55].

Nafisi et al. investigated the interaction between dsDNA and TP using UV spectroscopy. The binding constant of the TP-DNA complex was calculated as $1.7 \times 10^4\ M^{-1}$. Spectroscopic evidence showed that TP interacts with G-C and A-T nucleobases using mostly H-bonds. Johnson et al. investigated the DNA interactions of TP and TB using UV spectroscopy in the presence of Mg^{2+} and found out that TP and TB interact with all nucleobases (G-C and A-T) through H-bonding. Binding constants were calculated as 3.5×10^3 and $1.1 \times 10^3\ M^{-1}$, respectively. The empirical and theoretical parameters in this paper are in good agreement with the literature.

4. Conclusions

Xanthine, theophylline, and theobromine have structural similarities with each other. Evaluation of these biomolecules' interactions with dsDNA revealed that xanthine, theophylline, and theobromine interact with dsDNA by using similar trends but different affinities. Diffusion coefficients, surface concentrations, and standard heterogeneous rate constants were calculated for xanthine, theophylline, and theobromine in the absence and presence of DNA. These values were significantly reduced in the presence of DNA, indicating the formation of DNA complexes. Using CV and DPV techniques, binding constant values for XT-DNA, TP-DNA, and TB-DNA complexes were calculated at about 10^3–$10^4\ M^{-1}$ levels, indicating that each molecule does not interact between dsDNA base pairs. Stabilization energies obtained from NBO analyses are compatible with the formed H-bonds from docking monitoring. According to the calculated DFT parameters, E_{HOMO}, ΔE, and other global activity parameters suggest that the expected binding affinity order is TB > TP > XT. However, having a higher negative E_{LUMO} value and two more N—H type hydrogens compared to TP and TB allows XT to make more H-bonds with dsDNA as an H-donor. Molecular docking studies revealed that each molecule interacts via the minor grooves of dsDNA, using mostly hydrogen bonds.

CRediT authorship contribution statement

Alper Fitoz: Data curation, Software, Investigation, Writing – original draft, Writing – review & editing. **Zehra Yazan:** Data curation, Resources, Writing – review & editing, Supervision, Funding acquisition.

Declaration of competing interest

The authors declare that they have no known competing financial interests or personal relationships that could have appeared to influence the work reported in this paper.

Data availability

I have shared the supplementary file at the attach file step

Acknowledgments

We are thankful to the Ankara University Research Fund for financial support on project number 20L0430001.

Appendix A. Supplementary data

Supplementary data to this article can be found online at https://doi.org/10.1016/j.ijbiomac.2023.125961.

References

[1] A. Traversand, G. Muskhelishvili, DNA structure and function, FEBS J. 282 (2015) 2279–2295, https://doi.org/10.1111/febs.13307.
[2] K.M. Abu-Salah, et al., DNA-based applications in nanobiotechnology, J. Biomed. Biotechnol. (2010), 715295, https://doi.org/10.1155/2010/715295.
[3] W. Choi, E.S. Lee, Therapeutic targeting of DNA damage response in cancer, Int. J. Mol. Sci. 23 (2022) 1701, https://doi.org/10.3390/ijms23031701.
[4] K.W. Caldecott, et al., The threat of programmed DNA damage to neuronal genome integrity and plasticity, Nat. Genet. 54 (2022) 115–120, https://doi.org/10.1038/s41588-021-01001-y.
[5] B. Cheng, et al., Recent advances in DDR (DNA damage response) inhibitors for cancer therapy, Eur. J. Med. Chem. 230 (2022), 114109, https://doi.org/10.1016/j.ejmech.2022.114109.
[6] I. Haq, Thermodynamics of drug–DNA interactions, Arch. Biochem. Biophys. 403 (2002) 1–15, https://doi.org/10.1016/S0003-9861(02)00202-3.
[7] C.S. Pundir, R. Devi, Biosensing methods for xanthine determination: a review, Enzym. Microb. Technol. 57 (2014) 55–62, https://doi.org/10.1016/j.enzmictec.2013.12.006.
[8] M. Dervisevic, et al., Construction of novel xanthine biosensor by using polymeric mediator/MWCNT nanocomposite layer for fish freshness detection, Food Chem. 181 (2015) 277–283, https://doi.org/10.1016/j.foodchem.2015.02.104.
[9] A. Fitoz, et al., Simultaneous trace electrochemical determination of xanthine theophylline and theobromine with a novel sensor based on a composite including metal oxide nanoparticle multi-walled carbon nanotube and nano-Na-montmorillonite clay, Electroanalysis 33 (2021) 2226–2234, https://doi.org/10.1002/elan.202100196.
[10] N.A. Nia, et al., Simultaneous determination of theobromine, theophylline, and caffeine using a modified electrode with petal-like MnO2 nanostructure, Talanta 222 (2021), 121563, https://doi.org/10.1016/j.talanta.2020.121563.
[11] B.R. Patel, et al., Simultaneous voltammetric detection of six biomolecules using a nanocomposite of titanium dioxide nanorods with multi-walled carbon nanotubes, Electrochim. Acta 362 (2020), 137094, https://doi.org/10.1016/j.electacta.2020.137094.
[12] A.B. Neef, et al., Metabolic labeling of DNA by purine analogues in vivo, ChemBioChem 13 (2021) 1750–1753, https://doi.org/10.1002/cbic.201200253.
[13] A. Mukherjee, W.D. Sasikala, Chapter one - drug–DNA intercalation: from discovery to the molecular mechanism, Adv. Protein Chem. Struct. Biol. 92 (2013) 1–62, https://doi.org/10.1016/B978-0-12-411636-8.00001-8.
[14] Y. Li, et al., Secondary structures, dynamics, and DNA binding of the homeodomain of human SIX1, J. Pep. Sci. 28 (2022), e3376, https://doi.org/10.1002/psc.3376.
[15] O.V. Mikolaichuk, et al., A new tetrazole-containing 2-amino-4,6-di(aziridin-1-yl)-1,3,5-triazine derivative: synthesis, interaction with DNA, and antitumor activity, Russ. Chem. Bull. 71 (2022) 1050–1056, https://doi.org/10.1007/s11172-022-3507-1.
[16] S. Khashkhashi-Moghadam, et al., Novel perspective into the interaction behavior study of the cyanidin with human serum albumin-holo transferrin complex: spectroscopic, calorimetric and molecular modeling approaches, J. Mol. Liq. 356 (2022), 119042, https://doi.org/10.1016/j.molliq.2022.119042.
[17] A. Sharifi-Rad, et al., Oil-in-water nanoemulsions comprising Berberine in olive oil: biological activities, binding mechanisms to human serum albumin or holo-transferrin and QMMD simulations, J. Biomol. Struct. Dyn. 39 (3) (2021) 1029–1043, https://doi.org/10.1080/07391102.2020.1724568.
[18] N. Marjani, et al., Evaluation of the binding effect and cytotoxicity assay of 2-Ethyl-5-(4-methylphenyl) pyramido pyrazole ophthalazine trione on calf thymus DNA: spectroscopic, calorimetric, and molecular dynamics approaches, Luminescence 37 (2) (2022) 310–322, https://doi.org/10.1002/bio.4173.
[19] N. Zare-Feizabadi, et al., Determining the interaction behavior of calf Thymus DNA with anastrozole in the presence of histone H1: spectroscopies and cell viability of MCF-7 cell line investigations, DNA Cell Biol. 40 (8) (2021) 1039–1051, https://doi.org/10.1089/dna.2021.0052.
[20] R. Taheri, et al., Exploring the HSA/DNA/lung cancer cells binding behavior of p-Synephrine, a naturally occurring phenyl ethanol amine with anti-adipogenic activity: multi spectroscopic, molecular dynamic and cellular approaches, J. Mol. Liq. 368 (2022), 120826, https://doi.org/10.1016/j.molliq.2022.120826.
[21] H. Maheri, et al., Glucokinase activity enhancement by cellulose nanocrystals isolated from jujube seed: a novel perspective for type II diabetes mellitus treatment (in vitro), J. Mol. Struct. 1269 (2022), 133803, https://doi.org/10.1016/j.molstruc.2022.133803.
[22] F. Kalhori, et al., Enzyme activity inhibition properties of new cellulose nanocrystals from *Citrus medica* L. pericarp: a perspective of cholesterol lowering, Luminescence 37 (11) (2022) 1836–1845, https://doi.org/10.1002/bio.4360.

[23] R.A. Darban, et al., Multi-spectroscopic and molecular modeling studies of interaction between two different angiotensin I converting enzyme inhibitory peptides from gluten hydrolysate and human serum albumin, J. Biomol. Struct. Dyn. 35 (16) (2017) 3648–3662, https://doi.org/10.1080/07391102.2016.1264892.
[24] N. Jadon, et al., Recent trends in electrochemical sensors for multianalyte detection – a review, Talanta 161 (2016) 894–916, https://doi.org/10.1016/j.talanta.2016.08.084.
[25] J. Sochor, et al., Electrochemistry as a tool for studying antioxidant properties, Int. J. Electrochem. Sci. 8 (2013) 8464–8489.
[26] M. Fojta, Electrochemical sensors for DNA interactions and damage, Electroanalysis 14 (2002) 1449–1463, https://doi.org/10.1002/1521-4109(200211)14:21<1449::AID-ELAN1449>3.0.CO;2-Z.
[27] A.E. Radi, et al., Electrochemical sensing of the interaction of the anti-infective agent pentamidine with DNA, Monatsh. Chem. 152 (2021) 167–173, https://doi.org/10.1007/s00706-020-02721-3.
[28] H. Mahmoudi-Moghaddam, et al., A new electrochemical DNA biosensor based on modified carbon paste electrode using graphene quantum dots and ionic liquid for determination of topotecan, Microchem. J. 150 (2019), 104085, https://doi.org/10.1016/j.microc.2019.104085.
[29] D.E. Bayraktepe, A voltammetric study on drug-DNA interactions: kinetic and thermodynamic aspects of the relations between the anticancer agent dasatinib and dsDNA using a pencil lead graphite electrode, Microchem. J. 157 (2020), 104946, https://doi.org/10.1016/j.microc.2020.104946.
[30] G.S. Garbellini, et al., Voltammetric determination of ciprofloxacin in urine samples and its interaction with dsDNA on a cathodically pretreated boron-doped diamond electrode, Anal. Methods 7 (2015) 3411–3418, https://doi.org/10.1039/C5AY00625B.
[31] I.G. David, et al., Pencil graphite electrodes: a versatile tool in electroanalysis, J. Anal. Methods Chem. (2017) 1905968, https://doi.org/10.1155/2017/1905968.
[32] A. Ebadi, et al., Design, synthesis, molecular modeling, and DNA-binding studies of new barbituric acid derivatives, J. Iran. Chem. Soc. (2022), https://doi.org/10.1007/s13738-022-02576-x.
[33] A.M. Abu-Dief, et al., Synthesis and intensive characterization for novel Zn(II), Pd (II), Cr(III) and VO(II)-Schiff base complexes; DNA-interaction, DFT, drug-likeness and molecular docking studies, J. Mol. Struct. 1242 (2021), 130693, https://doi.org/10.1016/j.molstruc.2021.130693.
[34] I.M. Johnson, et al., Spectral analysis of naturally occurring methylxanthines (theophylline, theobromine and caffeine) binding with DNA, PLoS One 7 (12) (2012), e50019, https://doi.org/10.1371/journal.pone.0050019.
[35] S. Nafisi, et al., Structural features of DNA interaction with caffeine and theophylline, J. Mol. Struct. 875 (2008) 392–399, https://doi.org/10.1016/j.molstruc.2007.05.010.
[36] K. Nemčeková, et al., Interaction of DNA and mononucleotides with theophylline investigated using electrochemical biosensors and biosensing, Bioelectrochemistry 123 (2018) 182–189, https://doi.org/10.1016/j.bioelechem.2018.05.004.
[37] A. Urçuk, et al., Kinetic and thermodynamic studies on the interaction between calf thymus DNA and food additive vanillin - electrochemical methods, J. Mol. Liq. 360 (2022), 119434, https://doi.org/10.1016/j.molliq.2022.119434.
[38] D. Ilager, et al., Development of 2D graphene oxide sheets-based voltammetric sensor for electrochemical sensing of fungicide, carbendazim, Chemosphere 303 (2022), 134919, https://doi.org/10.1016/j.chemosphere.2022.134919.
[39] A. Askari, et al., Impact of linker histone in the formation of ambochlorin-calf thymus DNA complex: multi-spectroscopic, stopped-flow, and molecular modeling approaches, Iran. J. Basic Med. Sci. 24 (11) (2021) 1568, https://doi.org/10.22038/IJBMS.2021.58829.13070.
[40] Z. Lu, et al., MOF-derived Co3O4/FeCo2O4 incorporated porous biomass carbon: simultaneous electrochemical determination of dopamine, acetaminophen and xanthine, J. Alloys Compd. 858 (2021), 157701, https://doi.org/10.1016/j.jallcom.2020.157701.
[41] R. Zhang, et al., Simultaneous electrochemical determination of dopamine, ascorbic acid and uric acid using poly(acid chrome blue K) modified glassy carbon electrode, Sensors Actuators B 138 (2009) 174–181, https://doi.org/10.1016/j.snb.2008.12.043.
[42] A. Erdem, M. Ozsoz, Electrochemical DNA biosensors based on DNA-drug interactions, Electroanalysis 14 (2002) 965–974.
[43] S. Rauf, et al., Electrochemical approach of anticancer drugs–DNA interaction, J. Pharm. Biomed. Anal. 37 (2005) 205–217, https://doi.org/10.1016/j.jpba.2004.10.037.
[44] Hanwell et al., Avogadro: an advanced semantic chemical editor, visualization, and analysis platform, J. Cheminformatics 4(2012) 17.
[45] M. Frisch, et al., Gaussian 09, Revision d. 01 201, Gaussian, Inc., Wallingford CT, 2009.
[46] M. Franco-Perez, et al., Revisiting the definition of the electronic chemical potential, chemical hardness, and softness at finite temperatures, J. Chem. Phys. 143 (2015), 154103, https://doi.org/10.1063/1.4932539.
[47] R. Parthasarathi, et al., Chemical reactivity profiles of two selected polychlorinated biphenyls, J. Phys. Chem. 107 (48) (2003) 10346–10352.
[48] G. Morris, et al., Autodock4 and AutoDockTools4: automated docking with selective receptor flexibility, J. Comput. Chem. 16 (2009) 2785–2791.
[49] D.S. Biovia, BIOVIA Discovery Studio, Dassault Syst'emes, 2020.
[50] S.K. Saha, P.A. Banerjee, Theoretical approach to understand the inhibition mechanism of steel corrosion by the two aminobenzonitrile inhibitors, RSC Adv. 5 (2015) 71120–71130, https://doi.org/10.1039/C5RA15173B.
[51] Z. Demircioğlu, et al., Theoretical analysis (NBO, NPA, Mulliken Population Method) and molecular orbital studies (hardness, chemical potential, electrophilicity and Fukui function analysis) of (E)-2-((4-hydroxy2-methylphenylimino)methyl)-3-methoxyph, J. Mol. Struct. 1091 (2015) 183–195, https://doi.org/10.1016/j.molstruc.2015.02.076.
[52] S.J. Jenepha Mary, et al., Molecular structure, NBO analysis of the hydrogen-bonded interactions, spectroscopic (FT–IR, FT–Raman), drug likeness and molecular docking of the novel anti COVID-2 molecule (2E)-N-methyl-2-[(4-oxo-4H-chromen-3-yl)methylidene]-hydrazinecarbothioamide (dimer) - quantum chemical approach, Spectrochim. Acta A Mol. Biomol. Spectrosc. 251 (2021), 119388, https://doi.org/10.1016/j.saa.2020.119388.
[53] L. Xiao-Hong, et al., Natural bond orbital (NBO) population analysis of para-substituted S-Nitroso-thiophenols, THEOCHEM 900 (2009) 50–54, https://doi.org/10.1016/j.theochem.2008.12.022.
[54] G.S. Khan, et al., Chemistry of DNA minor groove binding agents, J. Photochem. Photobiol. B Biol. 115 (2012) 105–118, https://doi.org/10.1016/j.jphotobiol.2012.07.003.
[55] I. Ahmad, M. Ahmad, Dacarbazine as a minor groove binder of DNA: spectroscopic, biophysical and molecular docking studies, Int. J. Biol. Macromol. 79 (2015) 193–200, https://doi.org/10.1016/j.ijbiomac.2015.04.055.